scientific reports

Check for updates

OPEN

The homodimerization domain of the StI repressor is crucial for efficient inhibition of mycobacterial dUTPase

Zoé S. Tóth[1,2,3]✉, Ibolya Leveles[1,2], Kinga Nyíri[1,2], Gergely N. Nagy[1,2], Veronika Harmat[4,5], Thapakorn Jaroentomeechai[6], Oliver Ozohanics[7], Rebecca L. Miller[6], Marina Ballesteros Álvarez[2], Beáta G. Vértessy[1,2]✉ & András Benedek[1,2]✉

The dUTPase is a key DNA repair enzyme in *Mycobacterium tuberculosis*, and it may serve as a novel promising anti-tuberculosis target. StI repressor from *Staphylococcus aureus* was shown to bind to and inhibit dUTPases from various sources, and its expression in mycobacterial cells interfered with cell growth. To fine-tune and optimize StI-induced inhibition of mycobacterial dUTPase, we aimed to decipher the molecular details of this interaction. Structural background of the complex between dUTPase and a truncated StI lacking the repressor C-terminal homodimerization domain has been described, however, the effects of this truncation of StI on enzyme binding and inhibition are still not known. Using several independent biophysical, structural and enzyme kinetic methods, here we show that lack of the repressor homodimerization domain strongly perturbs both enzyme binding and inhibition. We also investigated the role of a mycobacteria-specific loop in the StI-interaction. Our results show that removal of this loop leads to a ten-fold increase in the apparent inhibition constant of StI. We present a high-resolution three-dimensional structure of mycobacterial dUTPase lacking the genus-specific loop for structural insight. Our present data suggest that potent inhibition of mycobacterial dUTPase by StI requires the wild-type full-length protein context.

Mycobacterium tuberculosis is the causative agent of tuberculosis (TB), a disease which was responsible for more than 1.3 million deaths in 2022 according to the Global Tuberculosis Report (issued by the World Health Organization)[1]. The emergence of multidrug-resistant bacteria strains and the co-morbidity of TB and HIV causes an increasing problem in treatment of TB, therefore there is a great need for the development of new anti-TB drugs[1,2]. Key enzymes in physiologically essential pathways are among the prime targets for such novel anti-TB chemotherapeutics.

The interlinked nucleotide biosynthesis and genome integrity pathways are of crucial importance in all living organisms. Mycobacteria rely on a limited set of pyrimidine nucleotide biosynthesis routes[3] and the single pathway towards dTTP biosynthesis necessarily involves the enzyme dUTPase (2'-deoxyuridine 5'-triphosphate nucleotidohydrolase, or DUT). dUTPase plays a central role in regulation of the cellular dUTP/dTTP ratio by catalyzing the hydrolysis of dUTP into dUMP, the substrate of thymidylate synthase. dUTPase also prevents uracil incorporation into DNA. This is of key importance in preventing double-strand breaks and cell death, as increased uracil incorporation into DNA may hyperactivate the base excision repair process, a DNA repair enzyme machinery operating both in prokaryotic and eukaryotic cells[3–6]. Accordingly, dUTPase is essential in *Escherichia coli*[7], *Saccharomyces cerevisiae*[8] and in *Mycobacterium smegmatis*[9], the laboratory model strain of *Mycobacterium tuberculosis*. Therefore, inhibition of mycobacterial dUTPase may be a promising way for anti-TB drug development[9]. Importantly, mycobacterial dUTPases possess a genus-specific insert (sequence

[1]Institute of Molecular Life Sciences, HUN-REN Research Centre for Natural Sciences, Budapest, Hungary. [2]Department of Applied Biotechnology and Food Science, Faculty of Chemical Technology and Biotechnology, Budapest University of Technology and Economics, Budapest, Hungary. [3]Doctoral School of Biology, Institute of Biology, ELTE Eötvös Loránd University, Budapest, Hungary. [4]Laboratory of Structural Chemistry and Biology, Institute of Chemistry, ELTE Eötvös Loránd University, Budapest, Hungary. [5]HUN-REN-ELTE Protein Modelling Research Group, Hungarian Research Network, Budapest, Hungary. [6]Copenhagen Center for Glycomics, Department of Cellular and Molecular Medicine, University of Copenhagen, Copenhagen DK-2200, Denmark. [7]Department of Medical Biochemistry, Semmelweis University, Budapest, Hungary. ✉email: toth.zoe@ttk.hu; vertessy.beata@ttk.hu; benedek.andras@ttk.hu

alignment provided in Supplementary Figure S1) inducing a surface loop structure that has been shown to be essential for mycobacterial viability making it an important segment in potential drug development[9–11].

Stl, the staphylococcal repressor protein (UniProt: Q9F0J8) of staphylococcal pathogenicity islands (SaPIs) was proposed as a universal dUTPase interaction partner, as it is able to interact with multiple enzymes from trimeric and dimeric dUTPase enzyme families[12–21]. As a consequence of complex formation, the dUTPase activity is inhibited with various efficiency regarding different dUTPase homologues[12–16,20]. Complete (i.e. 100%) in vitro inhibition of dUTPase activity is only observable upon Φ11 phage dUTPase-Stl complex formation[12], an in vivo occurring interaction during Φ11 bacteriophage infection of *S. aureus* strains containing SaPIs[17]. It has been shown for several Stl-dUTPase complexes that a tyrosine-rich Stl peptide segment in the N-terminal domain of the Stl protein is inserted into the dUTPase active site, even mimicking some of the dUTPase substrate interactions[22]. Nevertheless, species-specific differences in Stl-dUTPase binding affinity and inhibition efficiency depend on additional interactions outside the dUTPase substrate binding pocket[14,21]. The high-resolution crystal structures for Stl-dUTPase complexes invariably contain only a truncated segment of Stl (Stl^{NT}) since full-length complexes did not yield diffracting crystals. In this truncated Stl protein, the C-terminal homodimerization domain of Stl is removed[20–22]. It is not yet described how this truncation of Stl affects its dUTPase inhibition efficiency.

Homotrimeric dUTPases share a high level of structural and residue conservation at their active site, preserving a common enzymatic mechanism[23]. Nevertheless, dUTPase regions beyond the active site are remarkably different in dUTPases encoded by various species[24,25]. The mycobacteria-specific surface loop of *Mycobacterium tuberculosis* DUT (MtDUT) (UniProt: P9WNS5) presents a distinct structural alteration from all other homotrimeric DUTs[26]. In the absence of these five amino acids long (A133-S137) sequence segment, substrate binding and enzymatic activity is only slightly perturbed (an approximate 10% decrease in MtDUT k_{cat} was observed in vitro), rendering the loop-lacking enzyme variant ($MtDUT^{\Delta loop}$) still functional. However, in vivo experiments suggested that the presence of this insert is still essential for the survival of *Mycobacterium smegmatis* for reasons yet unknown[9]. The A133-S137 insert is part of the C-terminal arm of MtDUT that forms an integral part of the enzyme active site[27] and may also modulate MtDUT-Stl interactions.

In the present study, we aimed to decipher the molecular mechanism of Stl inhibition on MtDUT. Towards this goal we applied structural and functional studies to dissect the contribution of the A133-S137 mycobacteria-specific insert of MtDUT, as well as the Stl C-terminal truncation to the MtDUT–Stl interaction.

Results

The truncated Stl^{NT} is a less potent inhibitor of MtDUT

To test the Stl C-terminal domain deletion effect on MtDUT-Stl interaction, we created an Stl^{NT} (Stl^{1-159}) construct, similar to the Stl^{N-ter} (Stl^{1-156}) previously used in DUT-Stl structural studies[20–22], that contains the tyrosine-rich region playing a central role in the interaction[14]. We also set out to analyse the role of the mycobacteria-specific 133-AGLAS-137 (A133-S137) insert using a previously established $MtDUT^{\Delta loop}$ loop deletion variant[9]. We simultaneously investigated the effect of these two missing structural segments on in vitro MtDUT inhibition efficiency using steady-state DUT enzyme activity measurements. Results in Fig. 1; Table 1 show the two key parameters of the inhibition: the inhibition efficiency (at 400 nM Stl concentration) and the apparent inhibition constant $K_{i,app}$. Full-length Stl (Stl^{WT}) inhibition of $MtDUT^{WT}$ provided (82 ± 3)% inhibition of DUT activity, in accordance with previous data[13]. In contrast, Stl^{NT} displayed a decreased $MtDUT^{WT}$ inhibition with a (47 ± 2)% inhibition efficiency.

The apparent inhibition constant $K_{i,app}$ clearly indicated that the most efficient effect is associated with the wild type full-length protein complexes. The 2 nM apparent inhibition constant observed for the Stl^{WT}-$MtDUT^{WT}$ complex is at least one order of magnitude higher than in any other combinations. Results therefore suggest that both the removal of the Stl C-terminal homodimerization domain and the genus-specific MtDUT loop negatively interfere with inhibition efficiency. These data suggest considerably weaker interaction with the truncated Stl form (Fig. 1; Table 1).

Absence of the MtDUT loop and truncation of Stl both decrease binding affinity

To complement the kinetic characterization with direct binding assays, we applied biolayer interferometry (BLI). It is important to remark that the K_D values of previously published BLI measurements characterising DUT-Stl interactions[21,22] did not reflect the true binding affinity, since in these experiments the DUTs were immobilized on the sensor and Stl was in solution. Using this measurement set-up, the dimerization of Stl competes with the binding of its monomeric form to dUTPase. This arrangement interferes with the determination of the correct binding constant for the Stl-DUT complex since Stl concentration comprises both the dimeric and monomeric Stl forms although only the monomeric Stl is capable to bind to dUTPase[28]. To avoid this complication, we applied a BLI measurement set-up in which the Stl variants (Stl^{WT} and Stl^{NT}) were immobilized onto the sensor.

The determined K_D value for the Stl^{WT}–$MtDUT^{WT}$ binding is in the order of picomoles, while the one for Stl^{WT}–$MtDUT^{\Delta loop}$ interaction is an order of magnitude higher. Data indicate that the binding affinity is one order of magnitude weaker if the mycobacteria-specific loop is missing (Table 2).

The truncation of Stl into Stl^{NT} caused two orders of magnitude increase in the K_D value as compared to the Stl^{WT}-$MtDUT^{WT}$ complex, arguing for a much weaker interaction. This difference of two orders of magnitude is also observable in case of the measured dissociation rate constants (k_{off} values), but the association rate constants remained in the same order of magnitude (Fig. 6; Table 2, see also Supplementary Table S2 and Supplementary Figures S3–S10).

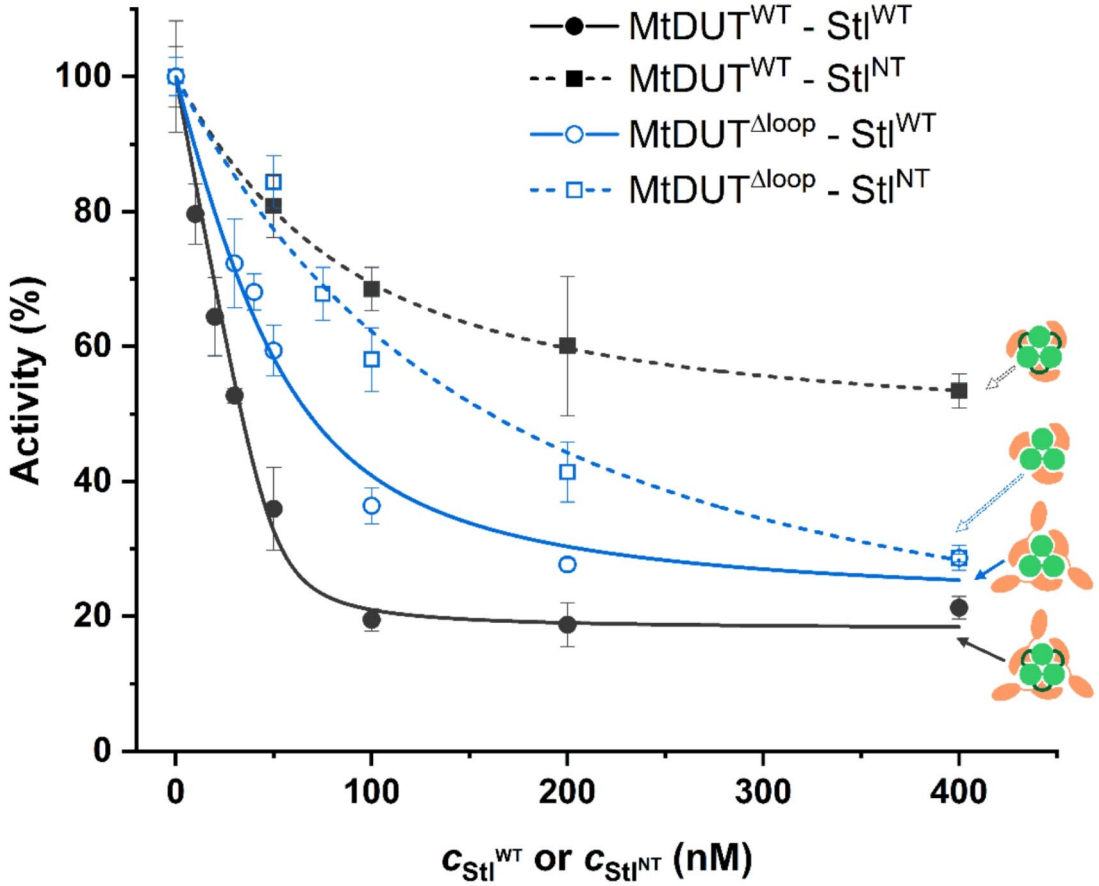

Fig. 1. Activity of MtDUT^{WT}and MtDUT$^{\Delta loop}$enzyme variants in presence of varying concentrations of Stl^{WT}and Stl^{NT}. Quadratic binding equation was fitted to the measured data from which apparent K_i values were determined. The fitted curves are shown in dark grey in case of MtDUT^{WT} and blue in case of MtDUT$^{\Delta loop}$. Curves showing MtDUT variants inhibited by Stl are solid lines, while the ones inhibited by Stl^{NT} are represented by dashed lines. Symbols representing the different MtDUT-Stl variant complexes consist of a light green dUTPase (with a dark green loop for the wild-type enzyme), Stl^{WT} and Stl^{NT} are shown in peach colour.

	$K_{i,app}$ (nM)	Inhibition of MtDUT activity*(%)
MtDUT^{WT} - Stl^{WT}	2.0 ± 1.2	82 ± 3
MtDUT^{WT} – Stl^{NT}	53.2 ± 4.6	47 ± 2
MtDUT$^{\Delta loop}$ - Stl^{WT}	21.1 ± 5.3	75 ± 4
MtDUT$^{\Delta loop}$ – Stl^{NT}	124.3 ± 33.1	72 ± 10

Table 1. Parameters of MtDUT enzyme activity inhibition by Stl^{WT} and Stl^{NT}. *At 400 nM inhibitor concentration.

MtDUT–Stl interaction may lead to different complex stoichiometries

We followed complexation of MtDUT and Stl using size-exclusion chromatography, as well. As shown on Fig. 2a, two peaks are observable on the chromatogram of the MtDUT^{WT}-Stl^{WT} complex. The peak elution volumes corresponding to these two peaks (11.1 ml, 13.0 ml) differ from the ones of the individual MtDUT^{WT} (14.8 ml) and Stl^{WT} (14.5 ml) (Supplementary Figure S16). It has been shown previously that human dUTPase and Stl^{WT} may form two types of complexes: in one case, three Stl molecules are attached to the trimeric dUTPase, whereas in the other case, only two Stl molecules are attached to the trimeric dUTPase[14]. Taking into account these previous findings, we suggest that the first complex peak in the size exclusion chromatography may correspond to a 3:3 binding stoichiometry, while the second peak, marked with an asterisk, may correspond to a lower,

Ligand	Analyte	K_D^* (pM)	k_{on} ($M^{-1}s^{-1}$) (10^5)	k_{off} (s^{-1}) (10^{-5})
Stl^{WT}	$MtDUT^{WT}$	< 1	2.70 ± 0.01	< 0.01 ± 0.01
Stl^{WT}	$MtDUT^{\Delta loop}$	33 ± 1	18.16 ± 0.01	5.99 ± 0.14
Stl^{NT}	$MtDUT^{WT}$	190 ± 1	5.42 ± 0.01	10.28 ± 0.04
Stl^{NT}	$MtDUT^{\Delta loop}$	Heterogenous binding		

Table 2. Complex formation kinetic parameters of Stl^{WT} and Stl^{NT} with $MtDUT^{WT}$ and $MtDUT^{\Delta loop}$. *χ^2 value was below 0.3 in all cases.

altered stoichiometry. The two types of complexes were only seen with the full-length proteins, and not in the case where Stl^{NT} binds to MtDUT (Fig. 2a). We propose that Stl^{NT} forms a complex of 3:3 binding stoichiometry with dUTPase, as seen in the crystal structures. We also suggest that steric hindrance may be involved in the formation of the 3:2 complex with full-length Stl and dUTPase, while in lack of the C-terminal Stl domain, the smaller Stl^{NT} protein can be better accommodated in the 3:3 complex.

To further investigate the stoichiometry of the $MtDUT^{WT}$–Stl^{WT} complex, we used native electrospray ionisation mass spectrometry (ESI-MS). A mass of 114.2 kDa was observed consistent with a complex where two Stl^{WT} molecules are attached to the trimeric dUTPase ($MtDUT^{WT}{}_3Stl^{WT}{}_2$ complex stoichiometry − 48.4 kDa for MtDUT trimer and 65.8 kDa for two Stl^{WT} monomers) (Fig. 2b). Using this method, we did not observe a molecular entity corresponding to the 3:3 stoichiometry.

Since we observed complex formation between $MtDUT^{WT}$ and Stl^{WT} with high affinity, it was also of interest to apply mass photometry, another independent method to assess complex formation in a low concentration range, as well. Mass photometry allows to analyse protein–protein interactions in a native-like state in solution, without immobilisation. We have found that a strong complex was formed using a stoichiometric mixture of the interaction partners each in 5 nM concentration (Fig. 2c). Based on the fact that in the mixture of the two proteins, one single complex peak is observed, the K_D value is estimated to be in nanomolar range.

In order to augment the present interaction analysis, we performed native gel electrophoresis analysis of $MtDUT^{WT}$–Stl^{WT} and $MtDUT^{WT}$–Stl^{NT} interaction (Fig. 2d, e). The results indicate that a distinct complex band appeared when $MtDUT^{WT}$ and Stl^{WT} are mixed at 3:3 and 3:2 ratios, with an additional presence of a small amount of Stl^{WT} single component. In contrast, no evident complex band is observed for the $MtDUT^{WT}$-Stl^{WT} 3:1 mixing ratio (Fig. 2d, Supplemetary Fig. S17b).

In case of the $MtDUT^{WT}$-Stl^{NT} interactions the 3:3 mixing ratio yielded a standalone complex band which is accompanied with smaller amounts of single components in the 3:2 sample. The 3:1 mixing also yielded both single component and complex bands (Fig. 2e, Supplementary Fig. S17a). Based on the native PAGE experiments we cannot discern MtDUT-Stl complexes with 3:3 and 3:2 stoichiometry.

Three-dimensional structure of the MtDUT–Stl^{NT} complex provides insights into the molecular basis of this interaction

To further explore the stoichiometry and molecular interactions of MtDUT-Stl complex, we performed high-throughput crystallization trials of the $MtDUT^{WT}$ mixed with either Stl^{WT} or Stl^{NT} with multiple screens and optimization scaffolds. Diffracting crystals were only obtained in the case of the MtDUT-Stl^{NT} sample thus, we determined the structure of this complex to 3.4 Å resolution (Supplementary Table S3).

The asymmetric unit of the $MtDUT^{WT}$-Stl^{NT} complex structure (PDB ID:8P8O) is composed of two DUT trimers facing toward each other via the bases of their three-fold symmetry central channel. Similarly to the previously published DUT-Stl^{N-ter} structural models[20–22], three Stl^{NT} monomers are bound to each of the DUT trimers, accounting for a 3:3 MtDUT-Stl^{NT} stoichiometry in the crystal (Fig. 3a, Supplementary Figure S11a). The MtDUT-Stl^{NT} interaction is fundamentally defined by the protrusion of the Stl^{NT} tyrosine-rich segment (Y106-D117) into the MtDUT active site mimicking DUT-substrate interactions, similarly as in[20–22] (Fig. 3b). Many MtDUT residues with a critical role in MtDUT-substrate interactions or catalysis[26](details in Fig. 3b with blue carbon colour code) are utilized for Stl^{NT} binding, likely contributing to $MtDUT^{WT}$-Stl^{NT} complex stability and precluding MtDUT-substrate interactions and enzymatic activity. Specifically, Lys91 residue of $MtDUT^{WT}$ forms hydrogen bonds with both Asp110 and Tyr113 residues of Stl^{NT}, which binds to the MtDUT active site pocket recognizing the substrate uracil ring[29]. $MtDUT^{WT}$ Tyr86, required for dUTP deoxyribose/ribose discrimination[29], forms a π-π stacking interaction with Tyr112 of Stl^{NT}, the catalytic base Asp83 ($MtDUT^{WT}$) forms hydrogen bond with the OH group of Tyr112, whereas $MtDUT^{WT}$ Arg64 interacts with Ser115 and Tyr116 of Stl^{NT}. Moreover, additional residues outside the MtDUT active site provide hydrogen-bond and polar interactions to Stl^{NT} tyrosine-rich segment (Fig. 3b with grey carbon color code for MtDUT residues; and Supplementary Table S4). Stl^{NT} interaction additionally induces conformational changes to the MtDUT N-terminal Ser18-Asp22 segment in the vicinity of the active site, which provides a prominent negatively charged surface region of MtDUT (Supplementary Fig. S11). Intriguingly, the mycobacteria-specific AGLAS loop of MtDUT is only partially resolved in the MtDUT-Stl^{NT} structure, whereas no electron density is present corresponding to the MtDUT C-terminal arm that folds over the DUT active site and has a decisive role in enzyme catalysis[30,31]. Since Stl^{NT} has shown different inhibition kinetics on $MtDUT^{WT}$ compared to the inhibition of $MtDUT^{\Delta loop}$ (cf. Fig. 1), the possibility has raised that the loop itself may play a steric role in C-terminal arm movements of $MtDUT^{WT}$.

The MtDUT^{WT}–Stl^{NT} complex structure (PDB ID:8P8O) shares notable similarities to a recently published MtDUT^{WT}-Stl^{N-ter} structure (PDB ID: 7PWX)[21], including the Stl-DUT 3:3 molecular arrangement and DUT:Stl interactions detailed above. Nevertheless, the MtDUT^{WT}–Stl^{NT} complex is crystallized in a different space group ($P2_12_12_1$) compared to MtDUT^{WT}-Stl^{N-ter} ($P2_1$), and accordingly, it also provides dissimilar structural features. In contrast to the MtDUT-Stl^{N-ter} structure, in the presented structure, the α5 helix of each Stl^{NT} monomer is found in an ordered conformation and is modelled in the electron density map. Within, His73 and Tyr70 from Stl^{NT} are packed against Pro15 and Tyr30 from MtDUT providing aromatic-proline and polar interactions, respectively, that supplement the MtDUT-Stl^{NT} complex interface in one of the MtDUT-Stl^{NT} subunit pairs (Fig. 3c).

Stl C-terminal domain (Stl^{CT}) is not present in the crystallized Stl^{NT} construct, nevertheless it modulates MtDUT-Stl interactions in solution studies (Figs. 1 and 2). To interrogate its potential role in complex formation, we generated multiple AlphaFold models including three copies of both MtDUT^{WT} and Stl^{WT}. The MtDUT^{WT}–Stl^{WT} Alphafold complex structures reproduce the overall 3:3 complex assembly found in the MtDUT^{WT}-Stl^{NT} crystal structure with the MtDUT^{WT} C-terminal arm dislodged by Stl. The MtDUT^{WT} C-term arm is found in a disordered ensemble with no molecular contacts with either Stl or MtDUT protein core (Supplementary Fig. S13). Intriguingly, the Stl^{CT} domains provide an additional trimer oligomerization surface, in all generated models, albeit the conformation of this additional assembly varies across the models. AlphaFold models of a MtDUT$^{\Delta loop}$-Stl^{WT} 3:3 complex are showing similar results (Supplementary Fig. S14).

The mycobacteria-specific surface loop of MtDUT^{WT} contributes to the stabilization of the enzyme C-terminal arm

To investigate how the mycobacteria-specific loop contributes to the MtDUT-Stl interaction, we additionally crystallized MtDUT$^{\Delta loop}$ together with the dUPNPP substrate analogue and determined their complex structure to 1.3 Å resolution (Supplementary Table S3). The MtDUT$^{\Delta loop}$ structure (PDB ID:8CGA) contains a single protomer in its asymmetric unit, that, together with its symmetry-related copies builds up an all-β jellyroll fold trimeric DUT assembly prototypical for MtDUT and trimeric dUTPases[23,32] (Fig. 3d). The MtDUT$^{\Delta loop}$ structure shares a high degree of overall similarity with MtDUT^{WT} (PDB ID: 2PY4) based on a root mean square deviation (RMSD) of 0.20 Å for 378 Cα atoms of the MtDUT trimers (Fig. 4a). The MtDUT$^{\Delta loop}$ structure features conserved interactions between dUPNPP and the enzyme core that are described for the MtDUT^{WT}-dUPNPP structure[30]. Namely, Lys91 and Asn77 residues form hydrogen bonds with the uracil ring of dUPNPP, Tyr86 forms van der Waals interactions with the deoxyribose, and Asp83 interacts with the 3'-OH of the deoxyribose with a hydrogen bond. The Mg^{2+}-chelated triphosphate moiety of substrate analogue is coordinated by Arg64, Ser65, Gly66, Gln113, and Arg135 (equivalent to Arg140 in MtDUT^{WT}) residues (Fig. 3e). In the MtDUT$^{\Delta loop}$ structure, the C-terminal arm is mostly disordered, in contrast to its ordered conformation when it is folded over the active site in MtDUT^{WT} (PDB ID: 2PY4). The last resolved residue of the polypeptide chain is Phe130, and beyond, only Arg135 from the 5th conserved motif could be modelled into the electron density, likely given its key contribution to nucleotide substrate binding and catalysis[33] (Figs. 3e and 4e). This indicates that the C-terminal arm is rendered more flexible in the absence of the mycobacteria-specific loop. Particularly, several polar interactions, H-bonds, and salt bridges that contribute to the stabilization of the C-terminal arm over the active site in MtDUT^{WT} (PDB ID: 2PY4), are abolished in MtDUT$^{\Delta loop}$ structure, due to the deletion of key participating residues and accompanying conformational changes (Fig. 4b, c, d). The absence of an ordered C-terminal arm remarkably changes the electrostatic surface of MtDUT$^{\Delta loop}$ compared to MtDUT^{WT}. The mostly positively charged active site and its surroundings become exposed in MtDUT$^{\Delta loop}$, as it is not shielded by the C-terminal arm (Fig. 4e, f).

To assess the conformation of the MtDUT C-terminal arm in the MtDUT$^{\Delta loop}$ structure, we compared AlphaFold models of MtDUT$^{\Delta loop}$ and MtDUT^{WT}. An ensemble of 10 MtDUT^{WT} models unanimously show that the C-terminal arm adopts a closed state (Supplementary Fig. S12a), similarly as seen in the MtDUT^{WT}-dUPNPP structure (PDB ID: 2PY4). In the MtDUT$^{\Delta loop}$ models the C-terminal arm is found with either in a closed state or in multiple different outward oriented poses, underscoring its apparent flexibility (Supplementary Fig. S12b).

Discussion

Our present kinetic and interaction analysis investigations of MtDUT-Stl complexes clearly indicate that the full-length Stl is a tightly binding, highly efficient inhibitor of MtDUT, whereas truncation of either protein negatively interferes with complexation (Figs. 5 and 6). We show that Stl^{CT}, the homodimerization domain of Stl[22] plays an important role in the complex formation and inhibition of the dUTPase enzymatic activity. The significant role of this homodimerization domain in the dUTPase complexation is a novel finding. It is also underlying the key importance of the fact that dissociation of the Stl^{WT} homodimer is essential for dUTPase binding and is also interfering with the Stl repressor function[12,28,34]. We also established that the mycobacteria-specific loop of MtDUT may modulate Stl complexation and MtDUT C-terminal arm conformation. As this segment is dissimilar from the human host dUTPase architecture, its structural consideration may assist the design of MtDUT-targeted anti-TB drugs.

Examining the structural function of the MtDUT A133-S137 mycobacteria-specific insert, we observed that its deletion renders the majority of the C-terminal arm disordered in the MtDUT$^{\Delta loop}$ crystal structure, suggesting an increased flexibility of this segment. Compared with MtDUT^{WT}, we concluded that this loop plays an important role in anchoring the enzyme C-terminal arm above the active site (Fig. 4b and c). In agreement with this, an earlier study investigating the MtDUT C-terminal arm movements using random acceleration molecular dynamics (RAMD) method revealed that residues 130–137 (including this insert region), and 149–

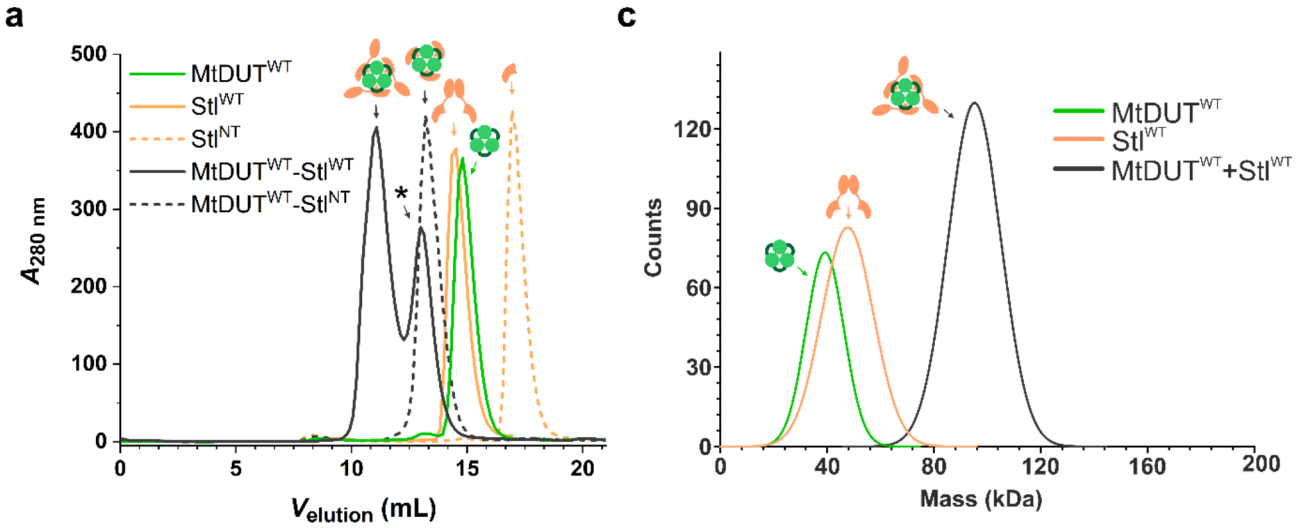

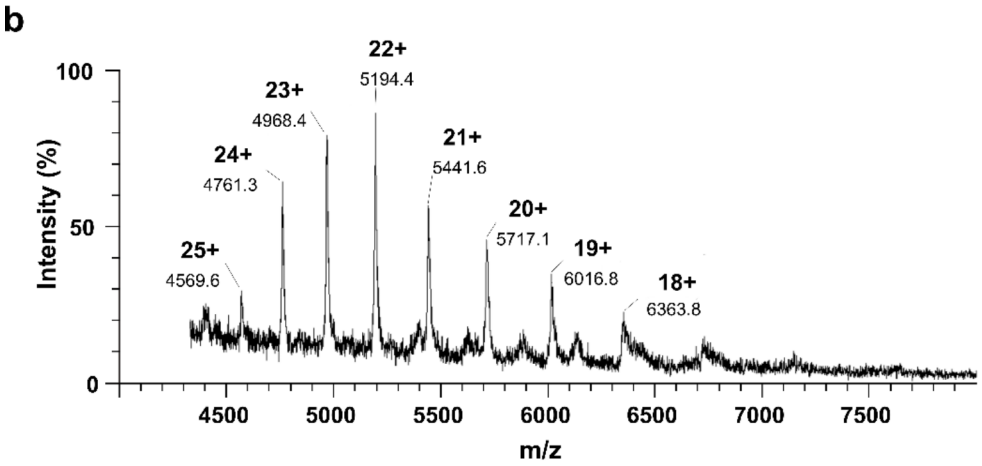

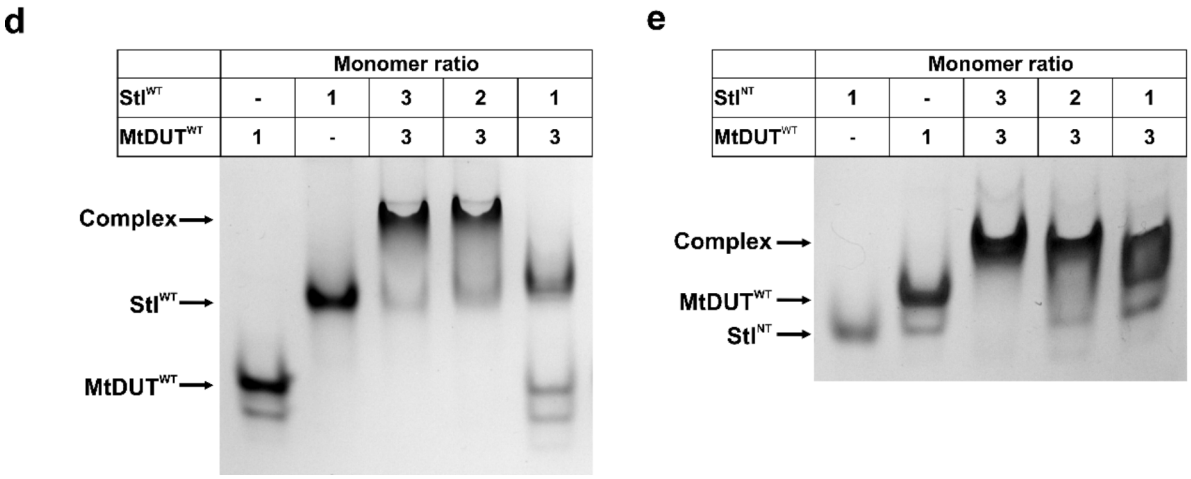

154 stay fixed to the enzyme core during the whole catalytic cycle, while the intercepted region (residues 138–148) comprising residues Arg140 and His145 shows much higher flexibility during repeated RAMD runs[35].

The inhibition efficiency of MtDUT activity using Stl^{WT} or Stl^{NT} as inhibitors, was only marginally altered by deletion of the A133-S137 insert in $MtDUT^{\Delta loop}$. Comparing the inhibition efficiency in the case of $MtDUT^{WT}$–Stl^{NT} and $MtDUT^{\Delta loop}$–Stl^{NT} reveals a limited inhibition efficiency for $MtDUT^{\Delta loop}$, which could be consistent with its increased arm flexibility that hinders effective Stl^{NT} interaction and inhibition.

The effect of deletion of the A133-S137 loop on MtDUT-Stl binding affinity is not fully conclusive based on our experiments. When Stl^{WT} is loaded on the sensor in the BLI experiments, the rate constant of complex dissociation is increased by several orders of magnitude in the case of the $MtDUT^{\Delta loop}$-Stl^{WT} complex, while the association rate constant shows a much smaller increase. These kinetic effects result in a weakened complexation, that may be related to the increased MtDUT C- terminal arm flexibility in $MtDUT^{\Delta loop}$. However, when either

◀**Fig. 2**. In solution complex formation of $MtDUT^{WT}$with Stl^{WT}or Stl^{NT}. (**a**) Size exclusion chromatography curves showing the chromatography of individual Stl^{WT}, Stl^{NT} and $MtDUT^{WT}$ and protein complexes. The curves showing chromatography of Stl^{WT} and Stl^{NT} proteins are presented in peach colour, as solid and dashed lines, with 14.5 ml and 16.9 ml peak elution volumes, respectively. The $MtDUT^{WT}$ curve is shown as a solid light green line with 14.8 ml peak volume. The curves corresponding to the protein-protein complexes are shown as solid and dashed dark gray lines, with 11.1 ml and 13.0 ml for the $MtDUT^{WT}$–Stl^{WT} complex and 13.2 ml elution peak volume for the $MtDUT^{WT}$–Stl^{NT} complex. The symbols showing the individual proteins, and the protein-protein complexes are similar to the ones presented in Fig. 1. (**b**) ESI-MS spectra of $MtDUT^{WT}$-Stl^{WT} mixture. The peak series of 4569 (with 25 + charge), 4761 (24+), 4968 (23+), 5194 (22+), 5442 (21+), 5717 (20+), 6017 (19+), 6364 (18+) indicate different charged states of a 114.200(± 0.080) kDa particle that corresponds to a complex with 3:2 binding stoichiometry. (**c**) Mass photometry histograms showing complex formation between $MtDUT^{WT}$ and Stl^{WT} or Stl^{NT}. The curves and figures corresponding to the individual proteins or the complex are similar to panel (**a**). (**d**-**e**) Native gel electrophoresis showing complex formation between $MtDUT^{WT}$ and Stl^{WT} (**d**), $MtDUT^{WT}$ and Stl^{NT} (**e**) at different mixing ratios.

$MtDUT^{WT}$ or $MtDUT^{\Delta loop}$ is loaded onto the sensor, the binding affinity is not significantly affected. This somewhat unclear effect of the absence of the A133-S137 loop is also due to the fact that in the case of interaction between MtDUT and Stl^{NT}, heterogeneous binding events prevent quantitative evaluation of the interaction affinity.

Theoretically, it seemed plausible that the shorter Stl^{NT} construct containing the tyrosine-rich region may inhibit MtDUT activity more effectively than Stl^{WT}, since the binding of a shorter protein could be more facilitated. On the contrary, we found that the truncation of Stl^{WT} to Stl^{NT} did not result in a more effective MtDUT inhibitor. In the crystal structure of $MtDUT^{WT}$-Stl^{NT} complex, each active site of the enzyme is blocked by a Stl^{NT}. Nevertheless, the strength of enzyme-inhibitor interaction was considerably reduced when Stl^{NT} was used. Thus, the C-terminal Stl domain (Stl^{CT}) has a direct or indirect effect in the formation of a stronger interaction, resulting in a more efficient inhibition of $MtDUT^{WT}$ activity. One possible explanation for this phenomenon is suggested by the AlphaFold models of $MtDUT^{WT}{}_3$:$Stl^{WT}{}_3$ complex, which show that an additional oligomerization surface is formed between C-terminal domains of Stl^{WT} monomers (Supplementary Fig. S13). This could provide an avidity effect, which may contribute to the formation of a stronger complex compared to $MtDUT^{WT}{}_3$:$Stl^{NT}{}_3$ complex. AlphaFold models for the $MtDUT^{\Delta loop}{}_3$:Stl_3 complex also show the potential avidity effect, however to a lesser extent (cf. Supplementary Fig. S14).

The C-terminal arm of homotrimeric DUTs is a flexible structural element whose active site interactions are critical for dUTP substrate binding and hydrolysis[27,36–38]. For both hDUT and MtDUT, it was suggested that there is a low probability of complete opening of the arm during substrate binding and product release, but it is more likely that several slightly altered conformations that are partially closed over the active site are adopted by the enzyme during catalysis[35,36].

Upon complex formation with Stl N-terminal domain constructs, the C-terminal arm of DUTs is displaced from the active site as seen in crystal structures of MtDUT-Stl^{NT}(PDB ID: 8P8O), MtDUT-Stl^{N-ter} (PDB ID: 7PWX)[21], Φ11 DUT-Stl^{N-ter} (PDB ID: 6H4C)[22], hDUT-Stl^{N-ter} (PDB ID: 7PWJ)[21] and lvDUT-Stl^{N-ter} (PDB ID: 7DLV)[20] complexes. All these structures display a trimer DUT state where all three active sites are occupied by the Stl N-terminal domain, thus this state is not compatible with DUT activity. In contradiction to this expectation, in vitro kinetic studies with numerous DUTs from different origins - except for the Φ11 phage DUT – invariably show 20–100% remnant enzyme activity in the presence of Stl[12–16,20]. One explanation for this observation might be that the C-terminal arm re-occupies the DUT active site to aid substrate hydrolysis. However, given the slow dissociation rate of Stl-DUT complexes and their tight interaction affinity[12], this scenario is not supported by the experimental data. An alternative explanation may suggest that not all of the active sites can be simultaneously occupied by Stl in solution. Accordingly, our gel filtration and ESI-MS studies of MtDUT-Stl^{WT} complex formation propose more than one binding stoichiometry, namely 3:3 and 3:2 MtDUT-Stl^{WT} complex stoichiometry. Small-angle X-ray scattering measurements of the hDUT–Stl complex also suggested the parallel presence of 3:3 and 3:2 DUT-Stl stoichiometry in solution[14]. Since full inhibition of MtDUT enzymatic activity requires all of its active sites to be blocked by the inhibitor, the potential presence of a complex with 3:2 binding stoichiometry will always result in remaining enzymatic activity.

Conclusions

Our present study creates the full and relevant framework for understanding the actual extent of inhibition that can be achieved in the interspecies DUT-Stl complexes. We wish to emphasize that using the full-length, wild-type proteins is essential in providing relevant information for the design of potent MtDUT inhibitors since the truncation of Stl, found to be essential to form a crystallizable protein complex, unfortunately led to a loss of crucial information about effective inhibition characteristics. In addition to performing experiments in the full-length Stl protein context, we also introduced an optimized experimental setup for the determination of strength of DUT-Stl complex formation, based on a relevant recent study from our laboratory[28]. In our present study, the binding affinity of the Stl: dUTPase complex has been determined in a correct experimental set-up using biolayer interferometry, and the data indicate the formation of an exceptionally strong complex of dUTPase and its protein inhibitor (K_D in the picomolar range). Due to the essential character of dUTPase, this robust complexation forms a promising basis for further inhibitor design. However, our results indicate that complete MtDUT inhibition is not achievable, neither by Stl^{WT} nor by Stl^{NT}. Further targeted engineering of Stl will be necessary to obtain Stl-based inhibitors that can eliminate mycobacterial DUT activity in vivo.

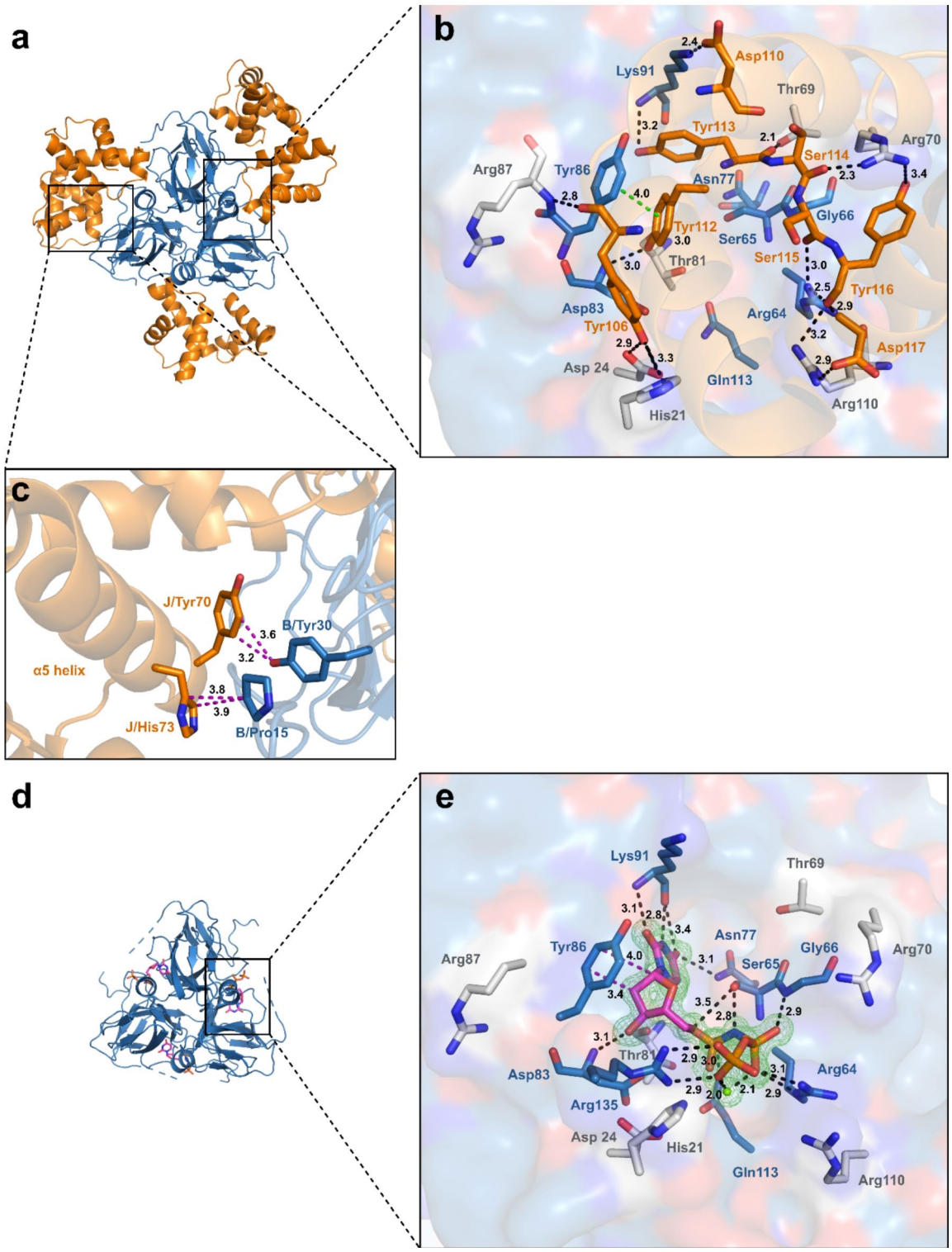

Materials and methods

Protein sequence comparison

The sequence comparison of several mycobacterial, other bacterial (based on sequence alignment in[9] and protein-protein BLAST search using https://blast.ncbi.nlm.nih.gov/Blast.cgi webserver), human and two Staphylococcal phage dUTPase sequences was carried out using Clustal Omega (https://www.ebi.ac.uk/jdispatcher/msa/clustalo). Afterwards, the multiple sequence alignment was fine-tuned manually.

Cloning and mutagenesis

Plasmid encoding Stl^{NT} Stl (UniProt: Q9F0J8) deletion mutant (Stl^{1-159}) was generated from Stl-encoding pGEX-4T-1 vector (GE Healthcare) by introducing a stop codon within the Stl sequence with site directed mutagenesis using partially overlapping Stl1-159_FW forward and Stl1-159_Rev reverse primers. $MtDUT^{WT}$

◀**Fig. 3**. Structure-based comparison of the MtDUT^{WT}-Stl^{NT}and MtDUT$^{\Delta loop}$–dUPNPP complexes. (**a**) Overall structure of MtDUT^{WT}–Stl^{NT} complex. MtDUT^{WT} is represented as blue cartoon, Stl^{NT} is represented as orange cartoon. (**b**) MtDUT^{WT} active site interactions with Stl^{NT}. Substrate analogue interacting residues are displayed as blue stick, while residues interacting only with Stl^{NT} are represented as grey sticks, Stl^{NT} interacting residues are shown as orange sticks. Interactions are indicated as dashed black (polar), π- π stacking interaction is shown as dashed green line (with distances measured in Å). (**c**) Interactions of Stl^{NT} α5 helix with MtDUT^{WT}. Interacting residues are shown as sticks. Colouring of the proteins are the same as in panel (**a**). Interactions are shown as dashed purple lines (with distances measured in Å). (**d**) Overall structure of MtDUT$^{\Delta loop}$ in complex with dUPNPP substrate analogue. MtDUT$^{\Delta loop}$ is displayed as blue cartoon, substrate analogue is represented as sticks. (**e**) Active site interactions of MtDUT$^{\Delta loop}$ in complex with dUPNPP. MtDUT$^{\Delta loop}$ is represented as surface. The representation of interacting residues is the same as on panel (**b**). The omit map around substrate analogue and Mg^{2+}-ion (green sphere) is contoured in green isomesh at 3.0σ level. Interactions are indicated as dashed black (polar) and purple (hydrophobic) lines (with distances measured in Å). Individual panels were created using PyMOL 2.5.4 (Schrodinger, LLC; https://www.pymol.org/). The figure was assembled using CorelDRAW 2020 (Corel Corporation; https://www.coreldraw.com).

(UniProt: P9WNS5) and MtDUT$^{\Delta loop}$ were amplified from pET-15b plasmid (Merck KGaA) using Avi-MtDUT_FW forward, Avi-MtDUT_Rev reverse primers and cloned to pAN4 vector (Avidity, LLC) in frame with Avi-tag, between XhoI and KpnI cleavage sites.

The Avi-tagged Stl constructs were created from Stl-encoding pGEX-4T-1 plasmid with the insertion of Avi-tag sequence on C-terminal end of GST-fused Stl sequence using Stl-Avi-mut-F-fin and Stl-Avi-mut-R-fin forward and reverse primers. Then GST-Stl-Avi was amplified using GST-Stl-Avi-pan4-F and GST-Stl-Avi-pan4-R primers and inserted into pAN4 vector between KpnI and XhoI restriction sites. The Stl^{NT}-Avi encoding gene was generated by mutagenesis of GST-Stl-Avi-encoding pGEX-4T-1 plasmid, afterwards cloned to pAN4 vector using GST-Stl-Avi-pan4-F and GST-Stl-Avi-pan4-R primers, resulting in the translation of a thrombin cleavable GST-tagged Stl^{NT}-Avi construct. The oligonucleotide primers used are listed in Supplementary Table 1.

Protein expression and purification

Proteins in this study were expressed in *E. coli* BL21 (DE3) Rosetta cells (Novagen, Merck KGaA) in LB media, induced by 0.5 mM Isopropyl β-D-1-thiogalactopyranoside after OD_{600} reached 0.5–0.6. The wild-type (WT), and Δloop mutant MtDUT enzymes were expressed from pET-15b vector for 4 h, at 37 °C. The genes encoding full-length Stl (Stl^{WT}) and Stl^{NT} proteins were expressed from pGEX-4T-1 plasmid for 4 h, at 30 °C. The cells were harvested by centrifugation for 30 min at 4 °C at 4000 rpm, then resuspended in precooled PBS and centrifuged for 30 min at 4 °C at 4000 rpm. The pellets were frozen and stored at -80 °C. The MtDUT and the Stl protein variants were purified similarly as previously described[13,26].

The MtDUT variant containing cell pellets were resuspended in 50 ml of lysis buffer (300 mM NaCl, 50 mM TRIS pH 8.0, 0.5 mM EDTA, 10 mM 2-mercaptoethanol, 1 mM PMSF, 5 mM benzamidine, 6.4 mM lysozyme and a cOmplete ULTRA EDTA-free protease inhibitor tablet (Roche)). The suspension was sonicated for 4 × 60 s and centrifuged for 30 min at 11,000 rpm at 4 °C. The supernatant supplemented with 15 mM imidazole and 1 mM $MgCl_2$ was applied onto a Ni-NTA column (Novagen) pre-equilibrated with lysis buffer. The column was washed with low salt, high salt buffers (30 mM KCl, 50 mM HEPES pH 7.5, 5 mM 2-mercaptoethanol and 300 mM KCl, 50 mM HEPES pH 7.5, 5 mM 2-mercaptoethanol respectively) and low salt buffer containing 50 mM imidazole to remove contaminants, the proteins were eluted with 500 mM imidazole dissolved in low salt buffer. The eluted samples were dialysed against buffer A (300 mM NaCl, 50 mM HEPES pH 7.5, 5 mM $MgCl_2$, 10 mM 2-mercaptoethanol), as a second purification step concentrated and gel-filtrated in buffer A on a Superdex 200 Increase 10/300 GL column (Cytiva).

The GST-tagged Stl protein variants containing cell pellets were resuspended in 30 ml Stl buffer (20 mM TRIS pH 7.5, 300 mM NaCl, 5 mM $MgCl_2$) supplemented with 0.1% Triton X-100, 2 mM dithiothreitol, one cOmplete ULTRA EDTA-free protease inhibitor tablet. The suspension was sonicated for 4 × 60 s and centrifuged for 30 min at 10,000 g at 4 °C. The supernatant was loaded to Glutathione Sepharose 4B resin (GE Healthcare) containing chromatography column pre-equilibrated with Stl buffer. Then the column was washed with 10 bed volumes of Stl buffer. The Stl variant was eluted by overnight cleavage of the GST-tag using 40 units of thrombin in 3 ml Stl buffer at 20 °C.

The Avi-tagged, biotinylated proteins used as sensor proteins for biolayer interferometry measurements were expressed in *E. coli* AVB101 cells (Avidity, LLC), which contain an inducible BirA gene coding pBirAcm plasmid allowing biotin ligase overexpression in THY media, and induced by 0.5 mM Isopropyl β-D-1-thiogalactopyranoside. The genes encoding Avi-MtDUT^{WT}, Avi-MtDUT$^{\Delta loop}$, Stl-Avi and Stl^{NT}-Avi proteins were expressed from a pAN4 vector for 4 h at 37 °C and 30 °C. Cells were harvested by centrifugation for 30 min at 4 °C at 4000 rpm, then resuspended in PBS and centrifuged again for 30 min at 4 °C at 4000 rpm. Then cell pellets were frozen and stored at -80 °C. The proteins were purified similarly as previously described, with the exception that the buffers used for the suspension and lysis of the pellets were supplemented with 50 mM biotin, and the cell suspension was incubated for 30 min at 4 °C, in order to allow biotinylation of Avi-tagged proteins.

Protein fractions collected during the purification processes were analysed by SDS-PAGE (Supplementary Figure S15). Protein concentrations were determined based on absorbance values measured at 280 nm by NanoDrop 2000c (Thermo Scientific).

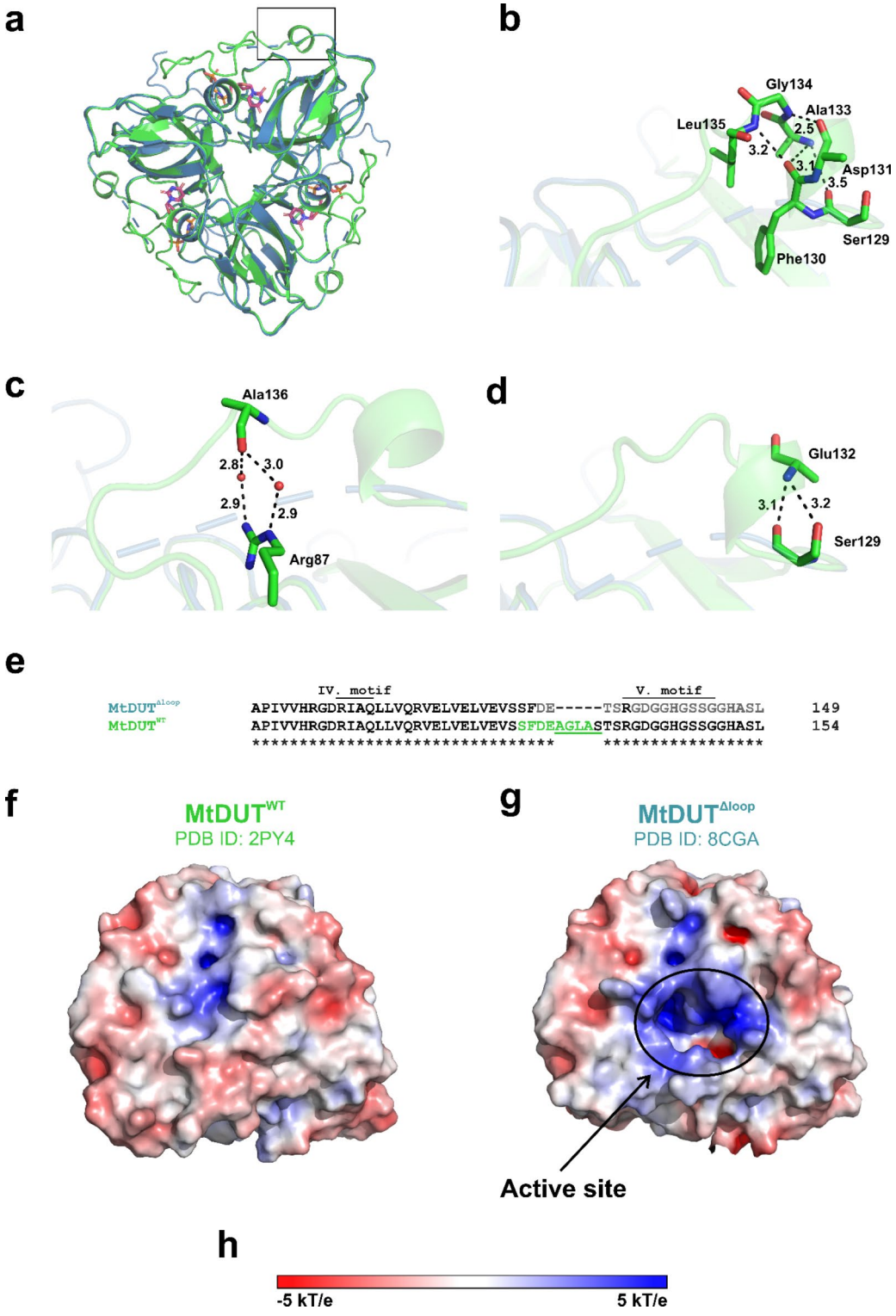

Biolayer interferometry

The kinetics analysis of complex formation between MtDUT enzyme variants (WT and and Δloop mutant) and Stl^{WT} and Stl^{NT} were carried out by biolayer interferometry using Octet K2 system (FortéBio) at 30 °C. For the equilibration of the high precision streptavidin biosensors (Sartorius), the record of Baseline and the dilution of sensor proteins, Stl buffer (20 mM TRIS pH 7.5, 300 mM NaCl, 5 mM $MgCl_2$) was used. The biotinylated Avi-tagged MtDUT or Stl protein variants were immobilised on the biosensor at 200 µg/ml or 60 µg/ml concentration respectively. The complex formation was investigated from both directions. The experimental setup was designed using Octet Data Acquisition software, the data analysis and the calculation of kinetics parameters (dissociation constant (K_D), association (k_a) and dissociation (k_d) rate constants) were performed using Octet Data Analysis software.

◀**Fig. 4**. Comparison of the MtDUT$^{\Delta loop}$ and MtDUT^{WT} structures. (**a**) Comparison of overall crystal structures of MtDUT^{WT} and MtDUT$^{\Delta loop}$. The wild-type enzyme is represented as light green cartoon, the surface loop lacking enzyme is shown as blue cartoon. The dUPNPP substrate analogue is shown as sticks. (**b**, **c**) Interaction network of amino acid residues forming the A133-S137 loop responsible for anchoring C-terminal arm. Interacting residues are shown as stick. Hydrogen bonds, salt bridges are shown as dashed black lines (with distances measured in Å). (**d**) Further anchoring interactions of the C-terminal arm that are resolved only in MtDUT^{WT} crystal structure. Interacting residues are shown as sticks, hydrogen bonds are represented as dashed black lines (with distances measured in Å). (**e**) Sequence alignment comparing the C-terminal segments of MtDUT$^{\Delta loop}$ and MtDUT^{WT}. The amino acid residues not resolved in the MtDUT$^{\Delta loop}$ structure are shown in grey, the residues highlighted in (**b**–**d**) panels are show in green. The AGLAS surface loop region is underlined in green. (**f**-**g**) Electrostatic potential of the molecular surfaces of MtDUT^{WT} (**f**) and MtDUT$^{\Delta loop}$(**g**) excluding the resolved region of the His6 epitope tag and the Met1 residue, to show a comparable structural region as MtDUT^{WT}. The position of the active site is highlighted with a circled area. (**h**) The colouring of the electrostatic surface potential scale. Individual panels (**a**–**h**) were created using PyMOL 2.5.4 (Schrodinger, LLC; https://www.pymol.org/), panel (**e**) was created and the figure was assembled using CorelDRAW 2020 (Corel Corporation; https://www.coreldraw.com).

DUT enzyme activity assay

Proton release during the dUTP hydrolysis was followed continuously in activity buffer (1 mM HEPES pH 7.5, 150 mM KCl, 5 mM $MgCl_2$ and 40 µM phenol red) at 559 nm at 20 °C using 10 mm path length cuvette[30,31]. The pH change during enzymatic reaction is minimal, which does not considerably affect the enzyme activity. The absorbance decrease as a function of time was detected using a Specord 200 (Analylitc Jena) spectrophotometer. The reaction was started with the addition of 10 µM dUTP after 5 min preincubation of 100 nM MtDUT enzyme variants with varying concentrations of Stl^{WT} or Stl^{NT} in activity buffer at 20 °C. Initial velocity (v_0) and turnover number (k_{cat}) were determined from the first 10% of the progress curve[12]. Stl^{WT} and Stl^{NT} inhibition data were fitted to the quadratic binding equation[13].

Crystallization and data collection, model building & refinement

The crystallization experiments were performed in 54-well sitting drop plates by vapor diffusion method. The initial crystallization conditions were screened in 96-well plates using PACT, JCSG +, Proplex (Molecular Dimensions) commercial reagents. The crystallization droplets were created by mixing the protein solution and the corresponding reservoir solution in a 1:1 volume ratio (0.5:0.5 or 1.0:1.0 µl), the reservoir contained 100 µl crystallization condition. The MtDUT-Stl^{NT} complex (protein 6.0 mg/ml) was crystallized with resevoir solution containing 20% PEG 4000, 0.1 M TRIS pH 8.0, wich was supplemented with 25% glycerol as a cryo-protectant before freezing in liquid nitrogen. The MtDUT$^{\Delta loop}$ enzyme variant (protein solution 13.5 mg/ml) crystals were grown in presence of 5 mM α,β-imido-dUTP (dUPNPP) with reservoir solution of 1.5 M Ammonium sulfate, 0.1 M TRIS pH 8.0, 12% glycerol. The diffraction data sets were collected from single crystals at 100 K on the XRD2 beamline of Elettra Sincrotrone Trieste at wavelength of 1.000 Å. Data were processed using XDS and XSCALE programs[39] in case of MtDUT^{WT}-Stl^{NT} complex. Resolution cutoff was based on CC1/2 > 0.3 criteria. The structure was solved by molecular replacement using MOLREP[40], the structures of *M. tuberculosis* DUT (PDB ID: 2PY4) and shrimp DUT in complex with Stl (PDB ID: 7DLV) as models. The data from measurement of MtDUT$^{\Delta loop}$ crystal were processed by iMosflm[41] and SCALA from CCP4 suite[42]. The structure was solved using MOLREP[40] and the structure of *M. tuberculosis* DUT (PDB ID: 2PY4) as a model. The model building and refinement were carried out with Coot[43] and Phenix[44] (versions 1.19.2_4158-000, 1.20.1_4487) softwares to determine the structures in both cases. The Ramachandran statistics of MtDUT^{WT}-Stl^{NT} complex structure are: 96.11% favoured, 3.82% allowed, 0.00% outliers. The Ramachandran statistics of MtDUT$^{\Delta loop}$ structure are: 99.28% favoured, 0.72% allowed, 0.00% outlier. The data collection and refinement statistics are shown in Supplementary Table S3. The crystal structures have been deposited in Protein Data Bank[45] under accession code 8P8O for MtDUT^{WT}-Stl^{NT} complex and 8CGA for MtDUT$^{\Delta loop}$.

Size exclusion chromatography

An AKTA FPLC purification system with a Superdex 200 Increase 10/300 GL column (GE Healthcare) was used for the size exclusion chromatography measurements. MtDUT^{WT}, MtDUT$^{\Delta loop}$, Stl^{NT} and Stl^{WT} proteins were gel filtrated individually and the 1:1 monomeric molar ratio of MtDUT variants with Stl^{WT} or Stl^{NT} were injected on the column in Stl buffer. Peak fractions of proteins and protein complexes were collected and analysed by SDS-PAGE, the peak elution volumes were plotted and compared.

Electrospray ionization mass spectrometry

A Waters QTOF Premier mass spectrometer (Waters, Milford, MA, USA) equipped with electrospray ionization source (Waters, Milford, MA, USA) operated in positive ion mode was used to study the MtDUT^{WT}-Stl^{WT} protein complex. Proteins were mixed in ca. 20 µM final concentrations and subjected to buffer exchange to 200 mM NH_4HCO_3 buffer applying Vivaspin® 500 Polyethersulfone centrifugal concentrators of 10 kDa weight cutoff. Mass spectra were measured under native conditions: the ions were generated from aqueous 50 mM NH_4HCO_3 buffer solution (pH 7.5) containing MtDUT^{WT}, Stl^{WT} or both protein constructs at ca. 0.5 µM monomer concentration. The capillary voltage was set to 2800 V, the sampling cone voltage was 25 V and the temperature of the source was kept at 80 °C. Collision cell pressure was 3.43 × 10-3 mbar and ion guide gas flow

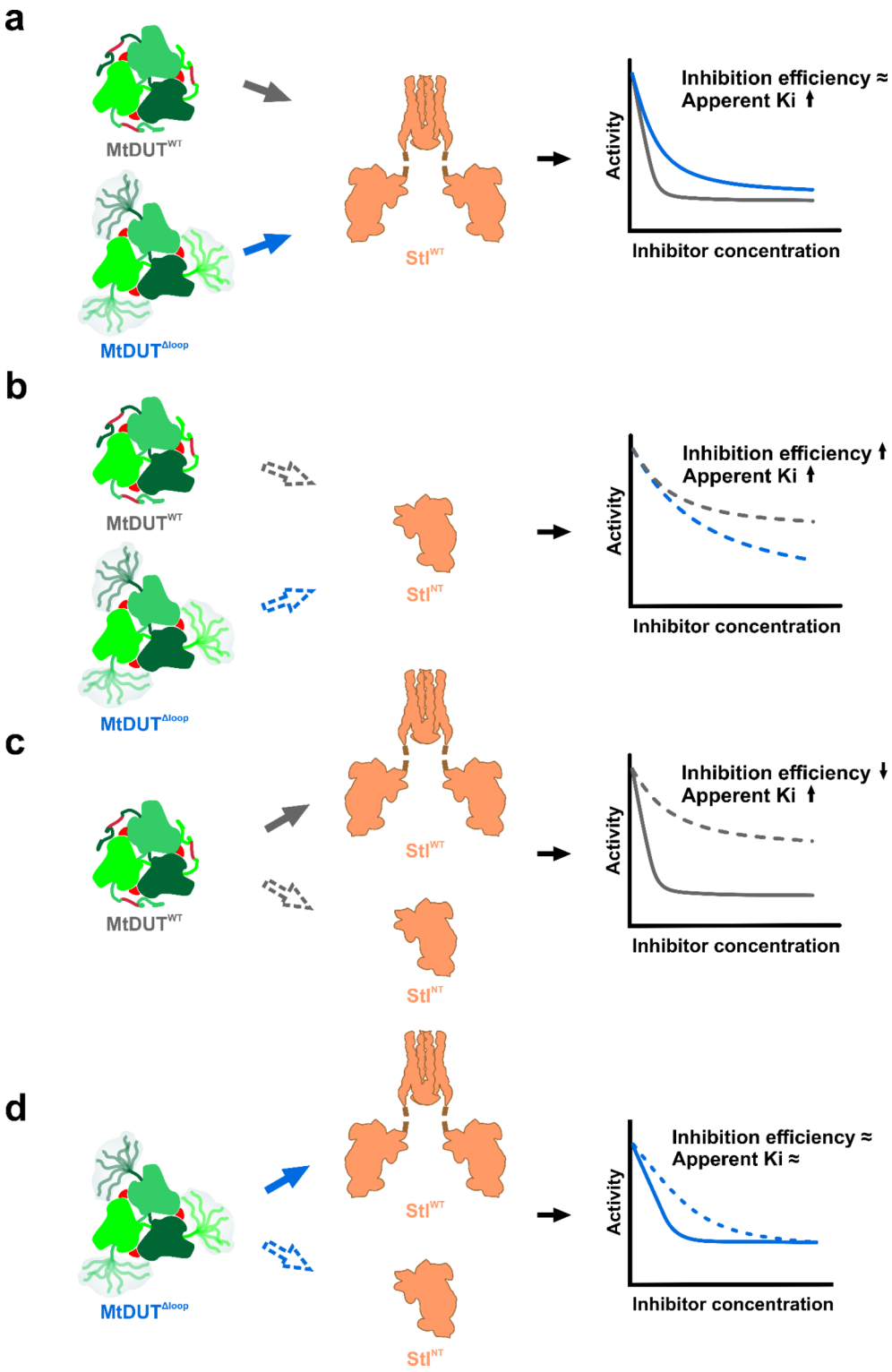

Fig. 5. The effect of different truncations on inhibitory potential of $Stl^{WT}$and Stl^{NT}exerted on $MtDUT^{WT}$and $MtDUT^{\Delta loop}$. (**a**–**d**) Schematic figures showing the different effects of Stl and MtDUT truncation on MtDUT activity. The steady-state activity curves are represented similarly as on Fig. 1. The representation of the molecules is the same as on Figure S2. Conclusions drawn regarding the inhibition efficiency and apparent inhibition constant (K_i) are related to $MtDUT^{WT}$ (on panel **a**, **b**) or to Stl (on panel **c**, **d**). Figure was created using CorelDRAW 2020 (Corel Corporation; https://www.coreldraw.com).

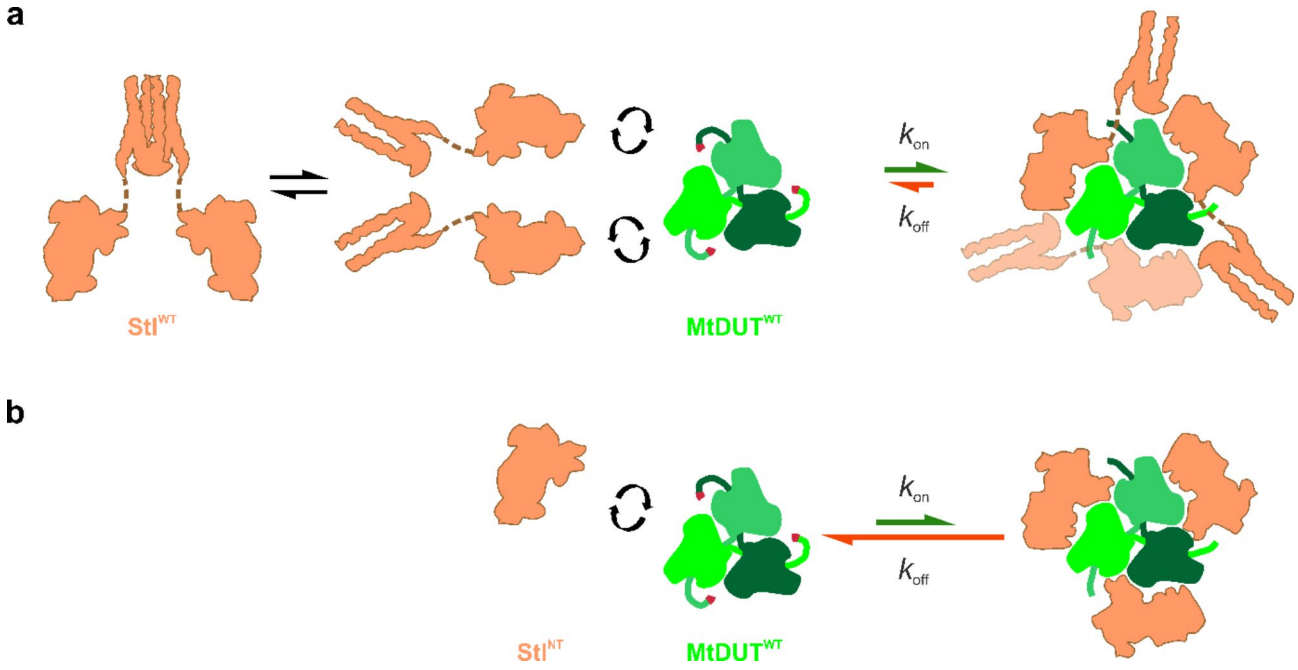

Fig. 6. Schematic representation of enzyme-inhibitor protein complex formation for the different truncated mutants. (**a**) MtDUT^{WT}-Stl^{WT} complex formation. (**b**) MtDUT^{WT}–Stl^{NT} complex formation. (**a**, **b**) The representations of the individual molecules are similar to the ones as on Figure S2. The protein-protein complexes are shown as the complexes of the individual proteins, which representations are based on MtDUT^{WT}-Stl^{NT} structural model (PDB ID: 8P8O), the exact conformation of the proteins and their binding stoichiometry are not taken into account. The magnitude of k_{on} and k_{off} values determined in the BLI measurements are represented as green and red arrows, respectively. Please note, that the dimensions of k_{on} and k_{off} values are different. Therefore, only the same kind of rate constants from the different complex formation reactions are comparable with each other. Figure was created using CorelDRAW 2020 (Corel Corporation; https://www.coreldraw.com).

was 35 ml/min. Mass spectra was recorded using the software MassLynx 4.1 (Waters, Milford, MA, USA) in the 1000–8000 m/z mass range.

Mass photometry analysis of complex formation

Microscope cover glasses (No 1.5 H, 24 × 50 mm, Paul Marienfeld GmbH, Lauda-Königshofen, Germany) were cleaned by sequential wash with MQ-water and HPLC-grade isopropanol, 5 times each, followed by drying in a nitrogen stream. Silicon gasket was then fixed on a clean cover glass. Mass calibration was performed for each experiment. Native protein marker (InvitroGen, San Diego, USA) was used to generate mass calibration curve consisting of proteins at MW 66, 146, 480, and 1048 kDa. Immediately prior measurements, protein stocks were diluted directly in Stl buffer (20 mM TRIS pH 7.5, 300 mM NaCl, 5 mM $MgCl_2$) to 100 nM concentration. Individual proteins and complexes were generally measured in mass photometry at 5 nM concentration. For each acquisition, a new well in a silicon gasket was used and 15-µL of sample was introduced into a well. Following autofocus stabilization, movie was recorded for 90s at room temperature. All data acquisition was performed using AcquireMP software (Refeyn Ltd, Oxford, UK) and data was analyzed using DiscoverMP (Refeyn Ltd, Oxford, UK). Data was presented as kernel density estimates with a 5 kDa bandwidth.

Native polyacrylamide gel electrophoresis

The native polyacrylamide gel electrophoresis measurements were carried out using 8% polyacrylamide gels pre-equilibrated with ELFO buffer (25 mM TRIS pH 7.9, 77 mM glycine) for 1.5 h at 150 V. The Stl^{WT} or Stl^{NT} protein samples were mixed with MtDUT^{WT} protein in 3:3, 2:3 and 1:3 mixing ratios based on monomer concentrations (4.5 µM: 4.5 µM, 3.6 µM:5.4 µM and 2.25 µM:6.75 µM for Stl^{WT}:MtDUT^{WT} mixtures and 9 µM:9 µM, 6 µM:9 µM and 3 µM:9 µM for Stl^{NT}: MtDUT^{WT} mixtures, respectively) and incubated on ice for 30 min. Then 15 µl of samples were loaded into each well and the electrophoresis was performed for 3 h at 150 V at 4 °C on ice.

Protein structure prediction

To further investigate the mobility of C-terminal arm of MtDUT^{WT} and MtDUT$^{\Delta loop}$ 10–10 models were generated using AlphaFold2[46,47]. The full-length MtDUT sequence (UniProt: P9WNS5) for MtDUT^{WT} and the same sequence lacking A133-S137 sequence element for MtDUT$^{\Delta loop}$ were used as an input with 3 copies. 5 relaxed models were generated in each run with template mode set to none. Structural models were superimposed for each enzyme variants.

To analyse the possible role of the C-terminal region of Stl^{WT} in interaction with MtDUT we used AlphaFold3[48] (https://alphafoldserver.com) as a prediction software. 5–5 models were generated using the full-length Stl^{WT} (UniProt: Q9F0J8), $MtDUT^{WT}$ (UniProt: P9WNS5) and $MtDUT^{\Delta loop}$ (UniProt: P9WNS5 lacking A133-S137 sequence element) sequences as input with 3–3 copies.

Protein–protein interaction analysis

The analysis of intermolecular interactions in $MtDUT^{WT}$-Stl^{NT} crystal structure (PDB ID: 8P8O) was performed using PDBePISA (https://www.ebi.ac.uk/pdbe/pisa/pistart.html)[49], and LigPlot + v.2.2.8[50] softwares.

Softwares used to create figures

BLI graphs were created using Octet Data Analysis software (FortéBio). The other graphs were created using Origin 2018 software. Gel images were captured using Image Lab 4.1 software (Bio-Rad). The illustrations of crystal structures were created using PyMOL 2.5.4 (Schrodinger, LLC), the structural superposition of crystal structures was carried out using align command in PyMOL, and electrostatic potential molecular surfaces were created using APBS Electrostatics Plugin[51]. Illustrations and creation of figures from individual graphs were prepared using CorelDRAW 2020 (Corel Corporation).

Data availability

The protein crystal structures have been deposited in Protein Data Bank under accession code 8P8O for MtDUTWT-Stl^{NT} complex and 8CGA for $MtDUT^{\Delta loop}$. Data supporting the findings of this study are available within the paper and its Supplementary Information.

Received: 8 March 2024; Accepted: 14 October 2024
Published online: 08 November 2024

References

1. Global tuberculosis report 2023. *Licence: CC BY-NC-SA 3.0 IGO* (World Health Organization, 2023).
2. Singh, V. & Chibale, K. Strategies to combat multi-drug resistance in tuberculosis. *Acc. Chem. Res.* **54**, 2361–2376 (2021).
3. Vértessy, B. G. & Tóth, J. Keeping uracil out of DNA: physiological role, structure and catalytic mechanism of dUTPases. *Acc. Chem. Res.* **42**, 97–106 (2009).
4. Goulian, M. et al. Mechanism of thymineless death. *Adv. Exp. Med. Biol.*, **195**(Pt B), 89–95 (1986).
5. Krokan, H. E., Drabløs, F. & Slupphaug, G. Uracil in DNA–occurrence, consequences and repair. *Oncogene*. **21**, 8935–8948 (2002).
6. Hirmondo, R., Lopata, A., Suranyi, E. V., Vertessy, B. G. & Toth, J. Differential control of dNTP biosynthesis and genome integrity maintenance by the dUTPase superfamily enzymes. *Sci. Rep.* **7**, 6043 (2017).
7. el-Hajj, H. H., Zhang, H. & Weiss, B. Lethality of a dut (deoxyuridine triphosphatase) mutation in Escherichia coli. *J. Bacteriol.* **170**, 1069–1075 (1988).
8. Gadsden, M. H., McIntosh, E. M., Game, J. C., Wilson, P. J. & Haynes, R. H. dUTP pyrophosphatase is an essential enzyme in Saccharomyces cerevisiae. *EMBO J.* **12**, 4425–4431 (1993).
9. Pecsi, I. et al. The dUTPase enzyme is essential in Mycobacterium smegmatis. *PLoS ONE*. **7**, e37461 (2012).
10. Horváti, K. et al. Antimycobacterial activity of peptide conjugate of pyridopyrimidine derivative against Mycobacterium tuberculosis in a series of in vitro and in vivo models. *Tuberculosis (Edinb)*. **95**(Suppl 1), S207–S211 (2015).
11. Nyíri, K. & Vértessy, B. G. Perturbation of genome integrity to fight pathogenic microorganisms. *Biochim. Biophys. Acta Gen. Subj.* **1861**, 3593–3612 (2017).
12. Szabó, J. E. et al. Highly potent dUTPase inhibition by a bacterial repressor protein reveals a novel mechanism for gene expression control. *Nucleic Acids Res.* **42**, 11912–11920 (2014).
13. Hirmondó, R. et al. Cross-species inhibition of dUTPase via the staphylococcal stl protein perturbs dNTP pool and colony formation in Mycobacterium. *DNA Repair. (Amst)*. **30**, 21–27 (2015).
14. Nyíri, K. et al. Structural model of human dUTPase in complex with a novel proteinaceous inhibitor. *Sci. Rep.* **8**, 4326 (2018).
15. Benedek, A., Pölöskei, I., Ozohanics, O., Vékey, K. & Vértessy, B. G. The stl repressor from Staphylococcus aureus is an efficient inhibitor of the eukaryotic fruitfly dUTPase. *FEBS Open. Bio*. **8**, 158–167 (2018).
16. Benedek, A. et al. The role of a key amino acid position in species-specific proteinaceous dUTPase inhibition. *Biomolecules*. **9**, (2019).
17. Tormo-Más, M. A. et al. Moonlighting bacteriophage proteins derepress staphylococcal pathogenicity islands. *Nature*. **465**, 779–782 (2010).
18. Dearborn, A. D. & Dokland, T. Mobilization of pathogenicity islands by Staphylococcus aureus strain Newman bacteriophages. *Bacteriophage*. **2**, 70–78 (2012).
19. Maiques, E. et al. Another look at the mechanism involving trimeric dUTPases in Staphylococcus aureus pathogenicity island induction involves novel players in the party. *Nucleic Acids Res.* **44**, 5457–5469 (2016).
20. Wang, F. et al. Structural basis of staphylococcal stl inhibition on a eukaryotic dUTPase. *Int. J. Biol. Macromol.* **184**, 821–830 (2021).
21. Sanz-Frasquet, C., Ciges-Tomas, J. R., Alite, C., Penadés, J. R. & Marina, A. The bacteriophage-phage-inducible chromosomal island arms race designs an interkingdom inhibitor of dUTPases. *Microbiol. Spectr.* **11**, e0323222 (2023).
22. Ciges-Tomas, J. R. et al. The structure of a polygamous repressor reveals how phage-inducible chromosomal islands spread in nature. *Nat. Commun.* **10**, 3676 (2019).
23. Takács, E., Grolmusz, V. K. & Vértessy, B. G. A tradeoff between protein stability and conformational mobility in homotrimeric dUTPases. *FEBS Lett.* **566**, 48–54 (2004).
24. Fiser, A. & Vértessy, B. G. Altered subunit communication in subfamilies of trimeric dUTPases. *Biochem. Biophys. Res. Commun.* **279**, 534–542 (2000).
25. Zang, K., Li, F. & Ma, Q. The dUTPase of white spot syndrome virus assembles its active sites in a noncanonical manner. *J. Biol. Chem.* **293**, 1088–1099 (2018).
26. Varga, B. et al. Active site of mycobacterial dUTPase: structural characteristics and a built-in sensor. *Biochem. Biophys. Res. Commun.* **373**, 8–13 (2008).
27. Varga, B. et al. Active site closure facilitates juxtaposition of reactant atoms for initiation of catalysis by human dUTPase. *FEBS Lett.* **581**, 4783–4788 (2007).

28. Nyíri, K., Gál, E., Laczkovich, M. & Vértessy, B. G. Antirepressor specificity is shaped by highly efficient dimerization of the staphylococcal pathogenicity island regulating repressors: stl repressor dimerization perturbed by dUTPases. *Sci. Rep.* **14**, 1953 (2024).
29. Chan, S. et al. Crystal structure of the Mycobacterium tuberculosis dUTPase: insights into the catalytic mechanism. *J. Mol. Biol.* **341**, 503–517 (2004).
30. Vertessy, B. G. Flexible glycine rich motif of Escherichia coli deoxyuridine triphosphate nucleotidohydrolase is important for functional but not for structural integrity of the enzyme. *Proteins*. **28**, 568–579 (1997).
31. Vertessy, B. G. et al. The complete triphosphate moiety of non-hydrolyzable substrate analogues is required for a conformational shift of the flexible C-terminus in E. coli dUTP pyrophosphatase. *FEBS Lett.* **421**, 83–88 (1998).
32. Nagy, G. N., Leveles, I. & Vértessy, B. G. Preventive DNA repair by sanitizing the cellular (deoxy)nucleoside triphosphate pool. *FEBS J.* **281**, 4207–4223 (2014).
33. Nagy, G. N. et al. Structural characterization of Arginine fingers: identification of an Arginine Finger for the pyrophosphatase dUTPases. *J. Am. Chem. Soc.* **138**, 15035–15045 (2016).
34. Nyíri, K. et al. HDX and native mass spectrometry reveals the different structural basis for interaction of the Staphylococcal pathogenicity island repressor Stl with dimeric and trimeric phage dUTPases. *Biomolecules*. **9**, (2019).
35. Lopata, A. et al. A hidden active site in the potential drug Target Mycobacterium tuberculosis dUTPase is accessible through small amplitude protein conformational changes. *J. Biol. Chem.* **291**, 26320–26331 (2016).
36. Tóth, J., Varga, B., Kovács, M., Málnási-Csizmadia, A. & Vértessy, B. G. Kinetic mechanism of human dUTPase, an essential nucleotide pyrophosphatase enzyme. *J. Biol. Chem.* **282**, 33572–33582 (2007).
37. García-Nafría, J., Timm, J., Harrison, C., Turkenburg, J. P. & Wilson, K. S. Tying down the arm in Bacillus dUTPase: structure and mechanism. *Acta Crystallogr. D Biol. Crystallogr.* **69**, 1367–1380 (2013).
38. Nord, J., Nyman, P., Larsson, G. & Drakenberg, T. The C-terminus of dUTPase: observation on flexibility using NMR. *FEBS Lett.* **492**, 228–232 (2001).
39. Kabsch, W. X. D. S. *Acta Crystallogr. D Biol. Crystallogr.* **66**, 125–132 (2010).
40. Vagin, A. & Teplyakov, A. Molecular replacement with MOLREP. *Acta Crystallogr. D Biol. Crystallogr.* **66**, 22–25 (2010).
41. Battye, T. G. G., Kontogiannis, L., Johnson, O., Powell, H. R. & Leslie, A. G. W. iMOSFLM: a new graphical interface for diffraction-image processing with MOSFLM. *Acta Crystallogr. D Biol. Crystallogr.* **67**, 271–281 (2011).
42. Agirre, J. et al. The CCP4 suite: integrative software for macromolecular crystallography. *Acta Crystallogr. D Struct. Biol.* **79**, 449–461 (2023).
43. Emsley, P., Lohkamp, B., Scott, W. G. & Cowtan, K. Features and development of Coot. *Acta Crystallogr. D Biol. Crystallogr.* **66**, 486–501 (2010).
44. Liebschner, D. et al. Macromolecular structure determination using X-rays, neutrons and electrons: recent developments in Phenix. *Acta Crystallogr. D Struct. Biol.* **75**, 861–877 (2019).
45. Berman, H. M. et al. The protein data bank. *Nucleic Acids Res.* **28**, 235–242 (2000).
46. Jumper, J. et al. Highly accurate protein structure prediction with AlphaFold. *Nature*. **596**, 583–589 (2021).
47. Mirdita, M. et al. ColabFold: making protein folding accessible to all. *Nat. Methods*. **19**, 679–682 (2022).
48. Abramson, J. et al. Accurate structure prediction of biomolecular interactions with AlphaFold 3. *Nature*. **630**, 493–500 (2024).
49. Krissinel, E. & Henrick, K. Inference of macromolecular assemblies from crystalline state. *J. Mol. Biol.* **372**, 774–797 (2007).
50. Laskowski, R. A. & Swindells, M. B. LigPlot+: multiple ligand-protein interaction diagrams for drug discovery. *J. Chem. Inf. Model.* **51**, 2778–2786 (2011).
51. Jurrus, E. et al. Improvements to the APBS biomolecular solvation software suite. *Protein Sci.* **27**, 112–128 (2018).

Acknowledgements

We are grateful for Edit Hirsch and for the Pharmatech Model Laboratory of Budapest University of Technology and Economics for providing opportunity to perform our BLI experiments. We acknowledge Elettra Sincrotone Trieste for providing access to its synchrotron radiation facilities and we thank Annie Heroux for assistance in using beamline XRD2. The authors thank Péter Tompa for the generous gift of pAN4 vector and E.coli AVB101 cells.

Author contributions

Study design: Z.S.T., A.B., K.N., B.G.V.Performed experiments: Z.S.T., A.B., K.N., I.L., O.O., T.J., M.B.A., R.L.M.Interpreted data: Z.S.T., A.B., K.N., I.L., G.N.N., V.H., B.G.V., T.J., R.L.M., O.O.Wrote article: Z.S.T., A.B., B.G.V., G.N.N.All authors reviewed the manuscript.

Funding

This work was supported by the National Research, Development and Innovation Office of Hungary (K135231, K146890, FK137867, 2018 – 1.2.1-NKP-2018-00005, 2022 – 1.2.2-TÉT-IPARI-UZ-2022-00003 to B.G.V., PD134324 to K.N.) and the TKP2021-EGA-02 grant, implemented with the support provided by the Ministry for Innovation and Technology of Hungary from the National Research, Development and Innovation Office. K.N. was also supported by the Parents Back to Science program of the Budapest University of Technology and Economics. G.N.N. was supported by the János Bolyai Research Scholarship of the Hungarian Academy of Sciences. The X-ray crystallographic study was also supported within projects No. VEKOP-2.3.2-16-2017-00014 and VEKOP-2.3.3-15-2017-00018 (to V.H), of the European Union and the Government of Hungary, co-financed by the European Regional Development Fund; as well as project no. 2018 – 1.2.1-NKP-2018-00005 of the National Research Development and Innovation Fund of Hungary, financed under the 2018 – 1.2.1-NKP funding scheme. This work was also supported by the European Molecular Biology Organization (EMBO) postdoctoral fellowship ALTF 336–2021 (to T.J.). The Novo Nordisk Foundation grant NNF22OC0073736 (to R.L.M.) and the Carlsberg Foundation CF20-0412 (to R.L.M.).

Declarations

Competing interests

The authors declare no competing interests.

Additional information

Supplementary Information The online version contains supplementary material available at https://doi.org/10.1038/s41598-024-76349-2.

Correspondence and requests for materials should be addressed to Z.S.T., B.G.V. or A.B.

Reprints and permissions information is available at www.nature.com/reprints.

Publisher's note Springer Nature remains neutral with regard to jurisdictional claims in published maps and institutional affiliations.